A Synchrotron X-ray Study of the Electron Density in YFeO₃

By D. du Boulay, E. N. Maslen and V. A. Streltsov*

Crystallography Centre, University of Western Australia, Nedlands 6907, Australia

and N. Ishizawa

Research Laboratory of Engineering Materials, Tokyo Institute of Technology, 4259 Nagatsuta, Midori-Ku, Yokohama 227, Japan

Abstract

Structure factors for synthetic yttrium orthoferrite, YFeO₃, measured with Mo $K\alpha$ (λ = 0.71073 Å) X-radiation and using a smaller crystal with focused λ = 0.75 Å synchrotron radiation are broadly consistent. Approximate symmetry in concordant difference densities indicates that cations deform the electron density more strongly than O atoms, although the deformation-density ($\Delta\rho$) map symmetry is lower than that expected from Fe cation interactions alone. The map's local symmetry is influenced strongly by the Y cations, but not by neighbouring O anions. Space group *Pnma*, orthorhombic, M_r = 192.76, a = 5.5877 (3), b = 7.5951 (4), c = 5.2743 (2) Å, V = 223.84 (2) Å³, Z = 4, D_x = 5.719 Mg m⁻³, $\mu_{0.75}$ = 29.82 mm⁻¹, $F(000)$ = 356, T = 293 K, R = 0.026, wR = 0.028, S = 5.4 (1) for the 1039 unique reflections of the synchrotron data set.

Introduction

Mobile cylindrical domains in low-coercivity materials such as the rare-earth orthoferrites, which propagate in a controlled manner, are required for shift-register-type memory devices. Although the magnetic characteristics of the rare-earth orthoferrites span a wide range, yttrium orthoferrite, YFeO₃, is a comparatively simple reference standard. In early research into magnetic bubble domain memories YFeO₃ was a convenient prototype, although its domains were too large for high-density storage.

YFeO₃ is essentially antiferromagnetic, but with weak ferromagnetism (T_N = 644 K); the Y cation is diamagnetic. Assessing the nature of the magnetic interactions, neglecting diamagnetic effects, the magnetic susceptibility is due only to the iron cation (Fe^{3+}, S = 5/2) array. The magnetic sub-structure in YFeO₃ can be described by two interpenetrating pseudo-cubic face-centred sublattices in which each Fe cation is octahedrally surrounded by six nearest-neighbour antiferromagnetic Fe atoms. Structurally YFeO₃ resembles CaTiO₃, for which the deformation density ($\Delta\rho$) was studied by Buttner &

Maslen (1992b). The perovskite-like CaTiO₃ structure is modified by octahedral tilting of the classification $a^-b^+a^-$, following Glazer (1972, 1975).

The crystal structure of YFeO₃, first studied by Geller & Wood (1956), was revised by Geller (1958) and Coppens & Eibschütz (1965). Analysis of possible space groups for the rare-earth orthoferrites by Marezio, Remeika & Dernier (1970a) strongly favours the centrosymmetric space group *Pbnm* (non-standard reorientation of *Pnma*), notwithstanding earlier attempts to refine structures using the non-centrosymmetric space group *Pbn2₁*.

Neutron scattering measurements by Tofield & Fender (1970) indicated that the room-temperature magnetic moments are approximately parallel to the *Pnma* [001] axis. Magnetic measurements by Goodenough & Longo (1970) and Demianets, Usov & Cherepanov (1976) established that the weak room-temperature ferromagnetism of YFeO₃, with its net moment directed along the [010] axis, results from a *ca* 0.5° spin canting between sublattices *via* Dzialoshinskii's (1957) antisymmetric super-exchange. Small spontaneous magnetizations of this type, first observed in α-Fe₂O₃, have been the subject of many studies. Polarized neutron studies of the ferromagnetic moment distribution in α-Fe₂O₃ by Nathans, Pickart, Alperin & Brown (1964) resemble that for MnCO₃ by Brown & Forsyth (1967) in that the magnetic cations' moment distribution deviates from spherical symmetry. Part of the MnCO₃ spin density was not localized near the magnetic atoms, being adjacent to the carbonate group. Reduction of the magnetic moment on Fe atoms in YFeO₃, also observed by Tofield & Fender (1970), was related to 'covalency' effects associated with s and p antibonding between Fe and its six O neighbours. The weak ferromagnetism is thus more complicated than a simple inclination of magnetic moments, which cannot be completely localized. Expansion of the radial density distribution of the 3d-orbital for Fe^{3+} in YFeO₃ compared with that in the free ion, similar to that for Mn^{2+} in MnCO₃, was also inferred from the magnetic measurements.

---

* Author to whom correspondence should be addressed.

As the spontaneous magnetic moment of *ca* 300 e.m.u. mol⁻¹ for YFeO₃ is larger than *ca* 57.6 e.m.u. mol⁻¹ for α-Fe₂O₃ and *ca* 188 e.m.u. mol⁻¹ for MnCO₃, more pronounced magnetic effects on structural parameters and charge density are expected. A study of the cation interactions in the relatively simple case of YFeO₃ may improve our understanding of the interactions in similar rare-earth orthoferrites where the rare-earth cations are paramagnetic.

Deformation densities for α-Al₂O₃ and α-Fe₂O₃ were studied by Maslen, Streltsov, Streltsova, Ishizawa & Satow (1993) and by Maslen, Streltsov, Streltsova & Ishizawa (1994), respectively. For α-Al₂O₃, the archetype for a special class within the perovskite series, the influence of the cation dominates the $\Delta\rho$ topography. Approximate sixfold $\Delta\rho$ symmetry near the Al cations for α-Al₂O₃ and near the Fe cations for α-Fe₂O₃ is higher than the threefold symmetry of the cation–oxygen bond geometry. Higher symmetry around cations, extending up to 6/*mmm* in the rhombohedral carbonates CaCO₃, MgCO₃ and MnCO₃, and topologically related perovskite-type structures (O'Keeffe & Hyde, 1977) were observed recently by Maslen, Streltsov, Streltsova & Ishizawa (1995). Such approximate $\Delta\rho$ symmetries, reflecting the strength of cation–cation interactions on the electron charge density, may also be relevant to our basic understanding of bonding and magnetic interactions in solids.

Ionic solids are often depicted as inter-penetrating arrays of negatively charged anions and positively charged cations with almost exclusive emphasis on the geometry of the anion array. Accurate synchrotron radiation diffraction imaging of the electron density in compounds with anion structural symmetry lower than that approximated by the cation lattice tests the reliability of that model.

Experimental

Crystals for the first study of YFeO₃ using tube Mo $K\alpha$ X-ray radiation (data set 1) were prepared by PbO flux growth (Remeika, 1956). 0.25 g of Y₂O₃, 0.177 g of Fe₂O₃ and 6.0 g of PbO were heated in a Pt crucible to 1580 K for 1 h, cooled at 30 K h⁻¹ to 1200 K and then quenched to room temperature. The heterogeneous mixture was simmered in dilute HNO₃ to dissolve the PbO. Possible lead substitution for Y in flux-grown YFeO₃ (Remeika & Kometani, 1968) was indicated by electron-beam-induced X-ray microanalysis to be negligible.

The crystal dimensions ranged from < 10 μm to 3 mm, larger specimens being dark with surfaces as reflective as polished metal. The smaller red translucent crystals tended to grow as extended rectangular rods. A rectangular prism-shaped single crystal (1) selected from this assembly was bounded by two {101}, two {010}, {10$\bar{1}$} and {$\bar{1}$01} faces with the dimensions 48 × 46 × 10.5 ×

9.5 μm, respectively, from the crystal centre. Two defect faces described by {$\bar{1}$04} and {$\bar{3}$02} indices spaced 27 and 14 μm from the crystal centre appeared as chamfered edges almost parallel to the longest dimension.

A study of optical spectra for YFeO₃ crystals grown by flux and hydrothermal methods (Kolb, Wood & Laudise, 1968) showed that Fe²⁺ occurred along with Fe³⁺ atoms in flux-grown crystals. In hydrothermally grown crystals all the iron was in the Fe³⁺ state. To assess the influence of crystal composition and mosaic structure on the measured $\Delta\rho$ topography, YFeO₃ crystals were prepared hydrothermally. Following Demianets (1978), crystals were precipitated from a solution of Y₂O₃ + Fe₂O₃ (0.2 wt %) – NaOH (53 wt %) in H₂O, in a sealed 2 ml gold tube (fill factor *ca* 0.7) inserted in an autoclave at 653 K for 10 d. Small red YFeO₃ crystals were removed after the tube was cut open. Crystal dimensions were measured and faces indexed using optical and scanning electron Philips SEM505 microscopes. The (crystal 2) specimen for synchrotron X-ray diffraction measurements was bounded by two {010}, two {101}, two {10$\bar{1}$} and {10$\bar{4}$} faces with dimensions 6 × 9 × 9 × 6 μm, respectively, from the crystal centre. The major faces of both crystals were those of a pseudo-ideal perovskite cubic cell. Geller & Wood (1956) observed that crystal habit in rare-earth orthoferrites and aluminates is influenced more strongly by the pseudo-cell than by the true crystallographic cell.

Diffraction intensity data set 1 was measured on a Syntex $P2_1$ four-circle diffractometer with Mo $K\alpha$ radiation (λ = 0.71073 Å) from an X-ray tube monochromated using a graphite-oriented monochromator in the equatorial setting.

Diffraction intensity data set 2 was measured with 0.7500 (2) Å synchrotron X-radiation using the BL14A four-circle diffractometer (Satow & Iitaka, 1989) at the Tsukuba Photon Factory. Vertically polarized synchrotron radiation from a vertical wiggler was monochromated by a double Si(111) crystal monochromator, and focussed using a curved mirror. The polarization ratio, *i.e.* the fraction of the total incident beam intensity with its electric vector vertical, is 0.95. An incident beam slit, 0.4 mm in diameter, installed before the monitor ion-counter, provides an intense and adequately homogeneous beam. By positioning the specimen slightly off-focus, changes in the synchrotron radiation intensity due to particle beam instabilities were minimized. Since the stored positron beam decays exponentially with time, an ion chamber was used to monitor the incident beam intensity. The alignment of the first monochromator crystal and of the vertical translations of the mirror were optimized automatically by flux maximization every 20 min during data collection. With this automatic optics optimization, the intensity of the incident beam is stable to within 1% over a 1 d period. A 3 × 3 mm receiving slit was placed in front of the scintillation counter.

Lattice constants for data set 1: $a = 5.594\,(2)$, $b = 7.601\,(2)$ and $c = 5.281\,(3)$ Å were from 14 reflections with 2θ values $30 < 2\theta < 44°$. Lattice constants for data set 2 were from three pairs of Friedel-related reflections at 2θ values of 64.95, 69.35 and 72.67°. Reflection intensities were measured systematically using $\omega/2\theta$ scans for a complete sphere of reciprocal space with $(\sin\theta/\lambda)_{max} = 1.080$ Å^{-1}, $-12 \le h \le 11$, $-16 \le k \le 16$, $-11 \le l \le 11$ for data set 1. Synchrotron intensity data (set 2), with $(\sin\theta/\lambda)_{max} = 1.021$ Å^{-1}, $-11 \le h \le 11$, $-15 \le k \le 15$, $-11 \le l \le 11$, were corrected for deadtime counting losses using the polynomial expansion by Hester, Maslen, Spadaccini, Ishizawa & Satow (1993). The NaI counter deadtime was measured to be 1.2 μs. Strong synchrotron intensities with count rates higher than 80 000 c.p.s. were reduced by Au foil with the attenuation factor 30.38. Six standard reflection intensities were remeasured every 100 reflections to monitor incident beam stability.

No reflections were classified arbitrarily as 'unobserved'. Measured intensities were modified and structure-factor variances from counting statistics were adjusted for source instability, as indicated by the standards (Rees, 1977). Variances consistent with Poisson statistics were retained. Those for the other reflections were increased according to the scatter of equivalents following a Fisher test. Further experimental details are set out in Table 1.

Lorentz and polarization corrections were applied. Absorption corrections (Alcock, 1974) were evaluated analytically. Linear absorption coefficients μ at Mo $K\alpha$ (31.99 mm^{-1}) and 0.75 Å were evaluated from atomic absorption coefficients listed in *International Tables for Crystallography* (1992, Vol. C). The reference state for all structure-factor calculations was the independent atom model (IAM) evaluated using spherical atomic scattering factors from *International Tables for X-ray Crystallography* (1974, Vol. IV), with dispersion corrections $\Delta f'$, $\Delta f''$ of -2.891, 3.580 at Mo $K\alpha$ and -2.914, 3.330 at 0.75 Å for Y; 0.345, 0.849 at Mo $K\alpha$ and 0.352, 0.931 at 0.75 Å for Fe; 0.0118, 0.0060 at Mo $K\alpha$ and 0.0121, 0.0068 at 0.75 Å for O, evaluated from *International Tables for Crystallography* (1992, Vol. C). All subsequent calculations utilized the *Xtal*3.2 system of crystallographic programs (Hall, Flack & Stewart, 1992) implemented on SUN SPARC and DEC 5000/120 workstations.

Before refining structural parameters, extinction correction of the full data sets based on intensities for symmetry-equivalent reflections with different path lengths (Maslen & Spadaccini, 1993) was attempted. The extinction parameter, included in Table 1, is significant for crystal 1, whereas that for crystal 2 is less than 3 e.s.d.s.

Atomic charges calculated subsequently from $\Delta\rho$ maps by Hirshfeld (1977) partitioning being negative for cations and positive for anions, suggest that the data set 1 structure factors were overcorrected for extinction.

Table 1. *Experimental and refinement data for* YFeO$_3$

	Crystal 1	Crystal 2
Radiation	Mo $K\alpha$	Synchrotron
λ (Å)	0.71073	0.7500 (2)
Diffractometer	Syntex $P2_1$	PF†
Monochromator	Graphite (002)	Si(111)
Scan speed (° min^{-1})	14	16
Peak scan width [$a + b\tan\theta$] (°)	1.8; 0.5	0.5; 0.0
Maximum 2θ (°)	100	100
Max. intensity variation of standards (%)	±(200), ±(040), ±(004) 1.7	±(800), ±(0 12 0), ±(008) 3.0
Reflections measured	8802	7452
Transmission range, min.; max.	0.126; 0.539	0.610; 0.718
Independent reflections; $F > 0$	1240; 1154	1047; 1039
Extinction,‡ r^*	0.29 (1) × 10^4	$|-r^*| < 3\sigma(r^*)$
Min. extinction y,§ (hkl)	0.80, (121)	No extinction applied
$R_{int}(F^2)$,		
Before	0.218	0.029
After absorption	0.108	0.024
Extinction applied	0.086	No extinction applied
R	0.054	0.023
wR	0.030	0.024
S	1.76 (4)	4.6 (1)
Max. shift/e.s.d.	0.2 × 10^{-3}	0.9 × 10^{-4}
Extinction ¶ refined, r^*	0.163 (9) × 10^4	0.39 (3) × 10^4
Min. extinction y,§ (hkl)	0.89, (121)	0.87, (002)
R	0.053	0.019
wR	0.027	0.021
S	1.60 (4)	4.06 (9)
Max. shift/e.s.d.	0.8 × 10^{-4}	0.9 × 10^{-4}
Separate extinction refinement,¶ r^*	0.60 (6) × 10^3	0.5 (2) × 10^3
Min. extinction y,§ (hkl)	0.95, (121)	0.98, (002 and 121)
R	0.055	0.026
wR	0.032	0.028
S	1.84 (4)	5.4 (1)
Max. shift/e.s.d.	0.6 × 10^{-4}	0.2 × 10^{-3}
$\Delta\rho$ min; max. (e Å^{-3})	-10.6; +4.6	-3.1; +2.8
$\sigma(\Delta\rho)$** (e Å^{-3})	0.9	0.1

† The BL14A four-circle diffractometer (Satow & Iitaka, 1989) at the Tsukuba Photon Factory, Japan.

‡ As proposed by Maslen & Spadaccini (1993).

§ $F_{obs} = yF_{kin}$, where F_{kin} is the value of the kinematic structure factor.

¶ Zachariasen (1967) extinction corrections included in least-squares structure refinement (Larson, 1970).

** Mean e.s.d. value (Cruickshank, 1949).

Alternative but biased extinction corrections can be evaluated by refining an extinction parameter as part of a least-squares optimization of the structural model. The widely invoked formula of Zachariasen (1967) was included in the structure refinement following Larson (1970). Extinction parameters determined for the two crystals by this approach indicated less extinction for crystal 1 than for crystal 2, in contrast with the estimates from symmetry-equivalent reflections (Table 1). The corresponding $\Delta\rho$ maps for the two data sets were dissimilar.

Systematic differences between observed and calculated low-angle structure factors may occur due to real characteristics of the electron density. Significant bias can occur in least-squares predictions if large differences between the observed data and model predictions are

Table 2. *Fractional coordinates and anisotropic vibration parameters* $(U \times 10^5 \text{ Å})$ *for* YFeO₃

Results for crystal 2 (SR) follow those for crystal 1 (Mo $K\alpha$) for each table entry.

	x	y	z	U_{11}	U_{22}	U_{33}	U_{12}	U_{13}	U_{23}
4 Fe on 4(b)	0	0	1/2	344 (17)	310 (15)	313 (15)	52 (13)	9 (15)	1 (16)
	0	0	1/2	280 (9)	338 (10)	287 (9)	45 (7)	8 (7)	−9 (7)
4 Y on 4(c)	0.06881 (7)	1/4	−0.01789 (7)	395 (13)	481 (11)	438 (11)	0	−48 (12)	0
	0.06852 (4)	1/4	−0.01787 (4)	445 (7)	666 (7)	531 (6)	0	−42 (5)	0
4 O1 on 4(c)	0.4600 (5)	1/4	0.1105 (5)	812 (118)	793 (91)	864 (92)	0	29 (74)	0
	0.4604 (3)	1/4	0.1103 (3)	451 (50)	310 (49)	466 (47)	0	−62 (38)	0
8 O2 on 8(d)	−0.3045 (4)	−0.0575 (3)	0.3075 (4)	735 (74)	878 (67)	892 (68)	−145 (61)	−128 (54)	94 (56)
	−0.3045 (2)	−0.0567 (2)	0.3076 (2)	335 (34)	618 (34)	395 (33)	−76 (29)	−105 (27)	70 (27)

more frequent than expected for a normal distribution, introducing artefacts into $\Delta\rho$ maps (Maslen, Streltsov, Streltsova, Ishizawa & Satow, 1993; Maslen, Streltsov, Streltsova & Ishizawa, 1994). The least-squares residuals for the YFeO₃ structure refinement were dominated by a few low-angle reflections with high weights. For the three strongest low-angle reflections $|F_o|$ is less than $|F_c|$, with $|F_o - F_c|/\sigma$ for synchrotron radiation (SR) data set 2 ranging up to 30. As the extinction parameter correlates strongly with the least-squares scale factor, the extinction parameter and scale factor adjust simultaneously to reduce the dominance of these residuals.

The excessive correlation that generates the problem was reduced by determining the scale and extinction parameters separately. Scale factors from the ordinate intercept of a Wilson plot of $\ln (I_o/I_c)$ *versus* $(\sin \theta/\lambda)^2$ were 0.54 (7) and 0.66 (4), whereas least-squares refinement of extinction with the structure parameters gave 0.440 (9) and 0.555 (3) for data sets 1 and 2, respectively. Values of 0.454 (3) (data set 1) and 0.582 (3) (data set 2), obtained by least-squares refinement of the scale, along with structure parameters excluding extinction, using unit least-squares weights except the eight reflections with $\sin \theta/\lambda < 0.2 \text{ Å}^{-1}$ which were omitted, were considered to be more reliable than those where high weights for the few extinction-affected reflections with $\sin \theta/\lambda < 0.2 \text{ Å}^{-1}$ ensured their dominance of the least-squares refinement.

With the scale fixed at the first stage value, extinction parameters were refined along with the structural parameters. For each data set 28 independent parameters, including all anisotropic vibration tensor elements, were determined by full-matrix least-squares refinement based on $|F|$ with weights equal to $1/\sigma^2(F_o)$ for all positive measured structure factors. The refined values are included in Tables 1 and 2.* Atomic charges and $\Delta\rho$ maps were calculated using the results of these refinements.

The greatly reduced crystal 1 extinction corrections at this last stage were less than 3 e.s.d.s, as indicated by the Maslen & Spadaccini (1993) algorithm for crystal

2 (Table 1). Being an unbiased estimator of structure-factor precision, this algorithm potentially provides a check on the values that minimize differences between observed and calculated structure factors. Unphysical corrections that might suggest inaccuracies in the measurement process could equally well indicate a non-uniform mosaic distribution that is beyond the scope of the simpler extinction correction algorithms.

A limited synchrotron X-radiation study supports the larger magnitude of the crystal 1 extinction corrections indicated by equivalent reflections. Intensity discrepancies for Friedel-related reflections increased with intensity, indicating significant dynamical effects for this crystal. The profiles for some reflections with the accurately collimated synchrotron beam were split, also indicating a discontinuous mosaic distribution. The small difference between the a and c unit-cell dimensions for this structure facilitates local interchange of cell axes that can distort the profile and hence affect the extinction. Interchange of lattice dimensions was reported by Geller & Wood (1956) for YFeO₃ and by Marezio, Remeika & Dernier (1970a) for RFeO₃, flux-grown crystals with R = La, Pr and Nd. These crystals exhibit multiple local twinning, but may also have large mosaics and consequently high extinction that is almost certainly direction-dependent, *i.e.* anisotropic. A more extensive study of crystal 1 with synchrotron X-radiation was not pursued because of these irregular profiles. This problem did not occur for the hydrothermally grown crystal 2. It is in this sense that hydrothermally grown crystals were classified as more 'perfect' in crystal growth studies by Demianets (1978).

The greater accuracy of the 0.75 Å synchrotron data set 2, indicated by the lower R values in Table 1, is partly due to improved counting statistics resulting from higher beam intensity, but a marked difference between the crystal 1 and 2 *meso*-structures is also indicated. Lower extinction corrections from equivalent reflections for crystal 2 are consistent with it being more ideally imperfect. Data set 2 is modelled more adequately by diffraction theory, which provides reliable extinction corrections in the case of uniform mosaic distributions that induce only limited extinction. Crystal 2 is therefore more suitable for accurate deformation-density imaging. The data set 2 results are correspondingly more significant.

---

* A list of structure factors for the two data sets has been deposited with the IUCr (Reference: AS0680). Copies may be obtained through The Managing Editor, International Union of Crystallography, 5 Abbey Square, Chester CH1 2HU, England.

Table 3. *Selected interatomic distances* (Å) *and angles* (°) *for* $YFeO_3$, *crystal* 2 *(SR)*

Y—Y^i	3.7148 (4)	Fe—Fe^{viii}	3.7975 (2)
Y—Y^{ii}	3.8786 (2)	Fe—Fe^{vii}	3.8419 (1)
Y—Y^{iii}	3.9739 (4)	Fe—O1^{iv}	1.9984 (6)
Y—Fe^{iii}	3.0703 (2)	Fe—O2^{ix}	2.003 (1)
Y—Fe^{iv}	3.1965 (2)	Fe—O2	2.027 (1)
Y—Fe	3.3487 (2)	O1—O1^{iv}	3.158 (3)
Y—Fe^v	3.7022 (3)	O1—O2^{ii}	2.789 (2)*
Y—O1^{iv}	2.233 (2)	O1—O2^{iii}	2.793 (2)*
Y—O1	2.291 (2)	O1—O2^x	2.870 (2)*
Y—O1^i	3.183 (2)	O1—O2^{xi}	2.899 (2)*
Y—O1^{vi}	3.465 (2)	O1—O2^{xii}	3.512 (2)
Y—O2^{vii}	2.275 (1)	O2—O2^{vii}	2.840 (2)*
Y—O2^{ii}	2.496 (1)	O2—O2^{xiii}	2.860 (2)*
Y—O2^{iii}	2.675 (1)	O2—O2^{xiv}	2.936 (2)
Y—O2	3.567 (1)	O2—O2^{xv}	3.102 (2)

Iron octahedra angles

O1^v—Fe—O2	87.88 (6)
O1^v—Fe—O2^{ix}	88.36 (6)
O2^{xiii}—Fe—O2^{xii}	89.62 (5)
O1^v—Fe—O1^{xvi} and O2^{xiii}—Fe—O2^{ix}	180 by symmetry
Fe^{iii}—O1—Fe^{xi}	143.7 (1)
Fe—O2—Fe^{vii}	144.81 (7)

Symmetry codes: (i) $x - \frac{1}{2}, \frac{1}{2} - y, -\frac{1}{2} - z$; (ii) $-x, \frac{1}{2} + y, -z$; (iii) $\frac{1}{2} + x, \frac{1}{2} - y, \frac{1}{2} - z$; (iv) $x, y, z - 1$; (v) $x - \frac{1}{2}, \frac{1}{2} - y, \frac{1}{2} - z$; (vi) $x - 1, y, z$; (vii) $-x - \frac{1}{2}, -y, z - \frac{1}{2}$; (viii) $-x, \frac{1}{2} + y, 1 - z$; (ix) $-\frac{1}{2} - x, -y, \frac{1}{2} + z$; (x) $1 + x, y, z$; (xi) $\frac{1}{2} - x, -y, z - \frac{1}{2}$; (xii) $-x, -y, 1 - z$; (xiii) $\frac{1}{2} + x, y, \frac{1}{2} - z$; (xiv) $x, -\frac{1}{2} - y, z$; (xv) $-1 - x, -y, 1 - z$; (xvi) $\frac{1}{2} - x, -y, \frac{1}{2} + z$.

* O—O distances in the FeO_6 octahedra.

Structural parameters

Structural geometries for rare-earth orthoferrites are fully described in earlier literature (*e.g.* Marezio, Remeika & Dernier, 1970*b*) and, for $YFeO_3$ particularly, by Coppens & Eibschütz (1965). Refined positional and vibrational parameters for both data sets are listed in Table 2, with selected crystal 2 bond lengths and Fe octahedra angles in Table 3.

The orthorhombic perovskite-like structure of $YFeO_3$ based on the SR crystal 2 refinement is depicted in Fig. 1. Atomic positions for the two crystals agree closely with those of Coppens & Eibschütz (1965) for $YFeO_3$, as expected from the standard deviations. The Y—O and Fe—O distances closely resemble values reported by these authors. The O—Fe—O angles deviate by small amounts from 90°. The three Fe—O distances range from 1.9984 (6) to 2.027 (1) Å for crystal 2. Since relatively small Y cations occupy interstices between the FeO_6 octahedra building blocks, the ideal cubic perovskite structure is stabilized by distorting the Y—O bonding polyhedron to form an orthorhombic structure. The ideal 12 O-atom polyhedron around Y becomes so distorted that the eight crystallographically independent Y—O distances, all equal in ideal perovskites, range from 2.233 (2) to 3.567 (1) Å (Table 3). Six nearest O atoms from the YO_{12} polyhedron form a trigonal prism around Y, whereas the FeO_6 coordination remains almost octahedral, as indicated in Table 3.

In Table 3 the Y—O and O—O distances closely resemble their counterparts in $HoFeO_3$ (Marezio,

Remeika & Dernier, 1970*b*). The similarity of the Y and Ho orthoferrites, supported by their almost identical unit-cell parameters, confirms the close correspondence between Y^{3+} and Ho^{3+} crystal radii in these structures.

The average Fe—O and O—O distances of 2.011 of 2.844 Å, respectively, for the FeO_6 octahedron hardly vary in all rare-earth orthoferrites from Pr to Lu (Marezio, Remeika & Dernier, 1970*b*). The average Fe—O and O—O distances for the FeO_6 in $YFeO_3$ from Table 3 are 2.009 and 2.842 Å, respectively. This Fe—O distance is also close to the yttrium–iron garnet value of 2.017 Å (Bonnet, Delapalme, Fuess & Thomas, 1975), which in turn is similar to the 2.057 Å bond in the tetragonally distorted octahedral Fe coordination in hematite (Maslen, Streltsov, Streltsova & Ishizawa, 1994). The average Fe—O distance is thus insensitive to distortions of the perovskite-like lattice in corundum-like structures, which are competitive when the smaller Fe atom replaces Y.

These Fe—O—Fe angles relevant to magnetic superexchange interaction are included in Table 3. Buckling of the corner-shared octahedra (Fig. 1) changes the Fe—O—Fe angle from the ideal value of 180°.

Vibration parameters

The more accurate data set 2 vibration ellipsoids for $YFeO_3$ are depicted at the 99% probability level in Fig. 1. Data set 2 vibration amplitudes are systematically lower for O atoms and higher for the Y atom than those
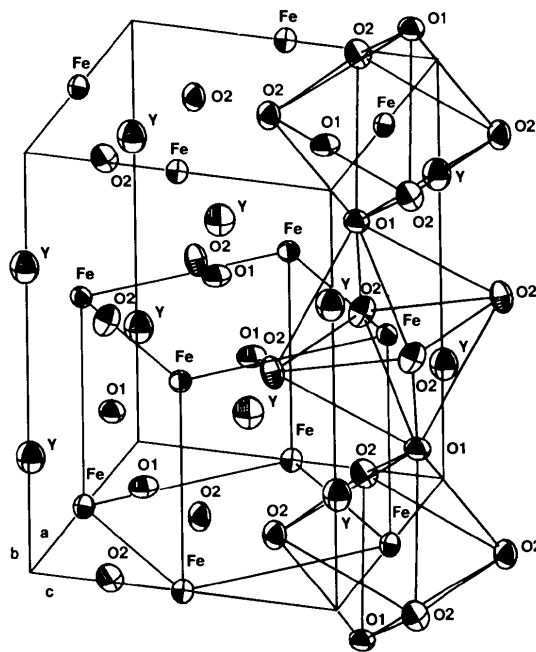

Fig. 1. Orthorhombic unit cell for $YFeO_3$. Vibrational ellipsoids at the 99% probability level.

from data set 1 (Table 2). This may be due to the lower statistical accuracy of high-angle crystal 1 reflections, reflected in relatively high parameter uncertainties.

The vibration parameters by Marezio, Remeika & Dernier (1970b) follow consistent trends spanning almost the whole RFeO$_3$ series. Transforming axes and converting from the β_{ij} values reported to U_{ij} values, all diagonal β_{ij} values seem to be twice those in the customary formula relating β_{ij} to U_{ij}. The Fe and O vibration parameters from data set 2 are within 2 e.s.d.s of those for HoFeO$_3$, whereas the Y-atom vibration parameters are more than 1.5 times those for Ho. All other rare-earth element U_{ij} values are also systematically smaller, as expected from their higher masses.

The mean-square amplitudes for the Fe atom in Table 2 are significantly less than those for Y, as expected from the rigidity of the FeO$_6$ octahedron. Tight packing around the Fe atom indicated by small Fe—O distances is confirmed by low vibration tensor elements. The larger Y-atom vibrations, especially along **b**, as shown by the data set 2 parameters in Table 2, reflect the relatively long average Y—O contact length of 2.77 Å. This follows the trend in the Marezio, Remeika & Dernier (1970b) data for the rare-earth atom vibration parameters to change progressively from $U_{33} > U_{11} > U_{22}$ towards $U_{33} > U_{22} > U_{11}$ and then towards $U_{22} > U_{33} > U_{11}$ as the rare-earth radius reduces. R atoms with smaller radii move further from the **b** axis in the (010) plane and vibrate more strongly along the [010] direction; this vibration being especially pronounced for the lighter Y atom. The distorted structure that is packed tightly in the **b** direction along the —O1—Fe—O1—Fe— line is loosely packed along the —Y—Y— line parallel to **b**.

Both O atoms show significant vibration anisotropy, as shown in Table 2 for data set 2. The shortest Fe—O1—Fe interaction parallel to **b** (Fig. 1) markedly reduces the O1-atom vibration in the [010] direction, whereas the shortest Fe—O2—Fe interaction, approximately perpendicular to the **b** axis, reduces the O2-atom vibrations in the [100] and [001] directions. The O-atom vibration parameters for all rare-earth orthoferrites studied by Marezio, Remeika & Dernier (1970b) show the same trend.

Atomic charges

Atomic charges (Table 4) were determined by projecting $\Delta\rho$ onto atomic density basis functions (Hirshfeld, 1977). The signs of the charges for both data sets are consistent with electronegativities for all the atoms, suggesting electron transfer from Y and Fe cations towards the O anions. The crystallographically independent O-atom charges for each data set are concordant. Apparently significant differences between values for the two crystals reflect their sensitivity to extinction discussed above. As reported previously (Buttner &

Table 4. *Atomic charges in electrons from the Hirshfield partitioning of* $\Delta\rho$ *for* YFeO$_3$

	Crystal 1 (Mo $K\alpha$)	Crystal 2 (SR)
Y	0.2 (1)	1.78 (3)
Fe	1.0 (1)	0.40 (3)
O1	-0.2 (1)	-0.86 (3)
O2	-0.0 (9)	-0.66 (3)

Maslen, 1992a,b,c), atomic charges for perovskite structures are sensitive to extinction to a degree that increases with the atomic number of the atoms in the structure. Overestimated extinction corrections tend to reduce the polarity of the structure by increasing the electron count on the heavier atoms. Values obtained from the SR data set, assuming no extinction, appear physically reasonable, as indicated by the two independent approaches to extinction (Table 1), justifying confidence in the reliability of these charges.

Electron density

Deformation-density sections in the (010) plane through the Fe atoms, based on the last refinements described in Table 1 for both YFeO$_3$ crystals, are shown in Figs. 2(a) and (b). The 1.0 and 0.5 e Å^{-3} contour intervals for crystals 1 and 2, respectively, are not less than one and five times the $\sigma(\Delta\rho)$ values listed in Table 1. Figs. 2(a) and (b) illustrate the degree of correspondence between $\Delta\rho$ maps for different crystals, based on separate refinements with Zachariasen-type extinction corrections. The $\Delta\rho$ maps of crystal 1 provide a useful check on the more accurate maps of the SR data set, but uncomfortably high noise precludes an independent physical interpretation.

A ($\frac{1}{2}$00) section through the Fe atoms for crystal 2 is shown in Fig. 3. The Y atom deviates from the plane shown by –0.38 Å. A section through the FeO$_4$ unit containing the Fe–O1 and the longer Fe–O2 vectors for crystal 2 is shown in Fig. 4.

In both Fig. 2 maps, $\Delta\rho$ density accumulates aspherically near the Fe atoms. It is directed away from near-neighbour anions in a manner typical of 3d electron density. The continuous positive $\Delta\rho$ density surrounding the Fe atom resembles that around the Mn cation in MnCO$_3$ (Maslen, Streltsov, Streltsova & Ishizawa, 1995). The $\Delta\rho$ topography may be related to expansion of the 3d orbitals with respect to the free atom with some possible contribution from the 4s orbitals, which agrees with magnetic scattering measurements. Defining Cartesian axes by the principal axes of the FeO$_6$ octahedron, the five 3d orbitals would be separated by an octahedral crystal field into two symmetry groups: two e_g orbitals are directed towards near-neighbour O anions. The three more stable t_{2g} orbitals are directed away from these atoms in a manner consistent with crystal-field theory. However, the local symmetry of the $\Delta\rho$ map around the Fe site approximates more closely to mmm, as seen in Figs. 2(a) and 3, which is higher than

the inversion centre expected from the exact structural geometry, but does not match the O-defined octahedral crystal field completely. Its correspondence with the arrangement of the nearest Fe cations contrasts with the lower symmetry of the O-atom positions projected in Fig. 2(a).

Further from the Fe atom sites the symmetry of the $\Delta\rho$ density is lower than that expected by considering interactions between the Fe cations alone. It is affected markedly by the Y cations, but not by the neighbouring O anions. This confirms the dominant effect of cation geometry on the $\Delta\rho$ symmetry.

The degree of asymmetry in the $\Delta\rho$ density near the Y site is markedly stronger than that near the Fe atoms. The local symmetry of the $\Delta\rho$ density near Y

corresponds to the crystallographic structural geometry, reflecting the strong influence of the low-symmetry (m) crystal field of the nearest six O atoms (Fig. 3). It might have been expected that the electron density surrounding a Y^{3+} cation with completely filled $4s4p$ orbitals be spherically symmetric. The zeroth-order approximation is based on a premise that deformation-density repopulation is dominated by near-degenerate orbitals. Studies of compounds containing rare earths, including La^{3+}, Gd^{3+} and Lu^{3+}, with closed subshell cores by Chatterjee, Maslen & Watson (1988), indicate that the spherical symmetry of the prepared state for these elements is not preserved when the atoms bind. In a perturbation expansion treatment of atomic charge density, polarization is
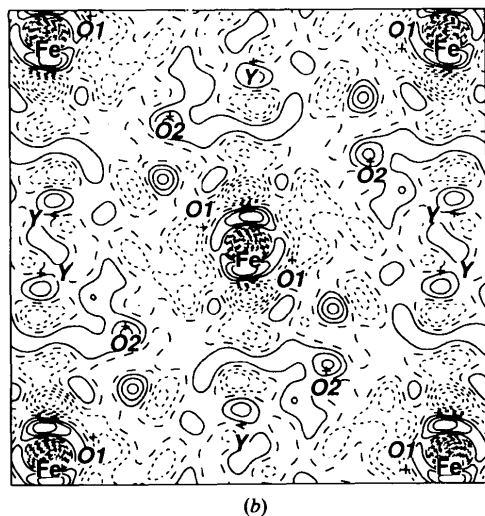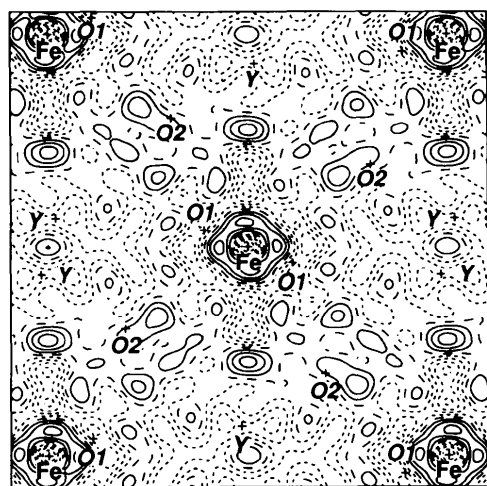

Fig. 2. $\Delta\rho$ for YFeO$_3$ in the (010) plane through Fe atoms. Atoms deviating from the plane by ±1.90 (Y and O1) and ±0.43 (O2) are shown in italics. (a) Crystal 2; (b) crystal 1. Map borders 6.3 × 6.3 Å. Contour intervals 0.5 and 1.0 e Å^{-3} for (a) and (b), respectively; positive contours solid, negative contours short dashes.
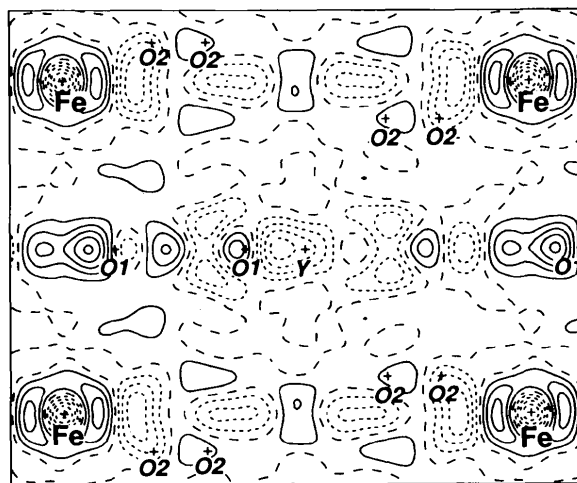

Fig. 3. $\Delta\rho$ for YFeO$_3$: crystal 2, plane ($\frac{1}{2}$00) through Fe atoms. Atoms deviating from the plane by -0.38 (Y), ±0.22 and -2.57 (O1) and ±1.09 and ±1.70 (O2) Å are shown in italics. Map borders 6.5 × 5.4 Å. Contours as for Fig. 2(a).
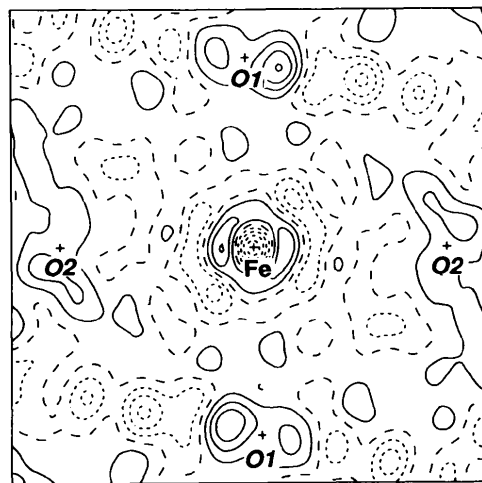

Fig 4. $\Delta\rho$ for YFeO$_3$: crystal 2, plane through Fe, O1 and O2 atoms. Map borders 5 × 5 Å. Contours as for Fig. 2(a).

described in terms of the repopulation of higher energy states. As the atomic number increases the energy gap to neighbouring levels decreases. The electron density appears to be redistributed significantly by polarization in such cases.

The $\Delta\rho$ density near the O atoms is depicted in Figs. 3 and 4. The more localized density around the O1 atom reflects the tighter contacts of O1 with Fe and Y atoms (Table 3). Excess electron density near the O1 atom is concentrated mainly along a line bisecting the Fe—O1—Fe angle, as shown clearly in Fig. 3. This is consistent with the requirements of a covalent contribution to a Fe—O—Fe superexchange interaction. The positive $\Delta\rho$ density near the O1 atom in Fig. 3 is also partly polarized along the shortest Y—O1 contact, 2.233 (2) Å in length. The O2 bonds to the cations are longer (Table 3) and the $\Delta\rho$ features around these atoms are more diffuse. The diffuse clouds around O2 are also polarized towards the closest Y cation and the Fe—Fe line, as is partly evident in Fig. 4. The $\Delta\rho$ topography again suggests Fe—O2—Fe superexchange interactions.

Discussion

Most magnetic scattering measurements for magnetically ordered solids have been discussed in terms of covalency parameters related to the simple molecular orbital (MO) model for transition metal salts (Forsyth, 1980). Covalency is associated with electron transfer from the ligands to the metal cations involving antibonding orbitals. The spin density exhibits spin transfer from the metal to the ligands. Metal magnetic moment reduction was mainly related to the MO parameters. The interpretations of some spin-density measurements included some spin-polarization and -correlation effects (e.g. Becker & Coppens, 1985). The main restriction in this model, which only includes the interaction of a magnetic cation with neighbouring ligands, is the omission of the interactions of the magnetic cations with each other.

The approximate high symmetry of the accurate synchrotron $\Delta\rho$ densities indicates that cations deform the electron density far more strongly than the O atoms. In YFeO₃, the most obvious effect of strong cation–cation interactions on the $\Delta\rho$ symmetry is on the distribution of the magnetic Fe atom, reflecting a pseudo-cubic metal-atom perovskite pattern. Cation–cation interactions have a significant effect on the structure and a dominant effect on the electron density. The spin-dependent effect remains significant well beyond normal bond lengths and may thus determine the nature of magnetic ordering and structural phase transitions. Electron density overlapping with the closed inner subshells of heavy cations is transferred by exchange to regions of lower electrostatic potential further from the nuclei. In this process anions can 'acquire' negative charges, although the extent of

the charge transfer can be questioned because the transferred density tends to retain the cations' symmetry. By penetrating the diffuse cation valence electron clouds the neutral anions are exposed to the nuclei shielded only by the inner shell electrons. Point charge representations of this phenomenon are misleading.

Emphasizing the cation point of view (O'Keeffe & Hyde, 1985), the YFeO₃ structure may be described as a pseudo-cubic metal-atom perovskite pattern with oxygen in the Fe₂Y₄ 'octahedral' sites (Fig. 1). The distortions may be represented as O-atom movement from the Fe—Fe edge; Fe remaining coordinated by six O atoms and Y having six near-neighbour O atoms at the corners of a trigonal prism. There is also a smaller relaxation of the Y cation positions.

References

ALCOCK, N. W. (1974). Acta Cryst. A30, 332–335.
BECKER, P. & COPPENS, P. (1985). Acta Cryst. A41, 177–182.
BONNET, M., DELAPALME, A., FUESS, H. & THOMAS, M. (1975). Acta Cryst. B31, 2233–2240.
BROWN, P. J. & FORSYTH, J. B. (1967). Proc. Phys. Soc. 92, 125–135.
BUTTNER, R. H. & MASLEN, E. N. (1992a). Acta Cryst. B48, 639–644.
BUTTNER, R. H. & MASLEN, E. N. (1992b). Acta Cryst. B48, 644–649.
BUTTNER, R. H. & MASLEN, E. N. (1992c). Acta Cryst. B48, 764–769.
CHATTERJEE, A., MASLEN, E. N. & WATSON, K. J. (1988). Acta Cryst. B44, 386–395.
COPPENS, P. & EIBSCHÜTZ, M. (1965). Acta Cryst. 19, 524–531.
CRUICKSHANK, D. W. (1949). Acta Cryst. 2, 65–82.
DEMIANETS, L. N. (1978). Hydrothermal Crystallization of Magnetic Oxides. Crystals for Magnetic Applications. Crystals – Growth, Properties, and Applications, edited by C. J. M. ROOIJMANS, Vol. 1, pp. 97–123. Berlin Heidelberg, New York: Springer-Verlag.
DEMIANETS, L. N., USOV, L. V. & CHEREPANOV, V. M. (1976). Inorg. Mater. 12, 603–606.
DZIALOSHINSKII, E. I. (1957). Sov. Phys. JETP, 5, 1259–1271.
FORSYTH, J. B. (1980). In Electron and Magnetization Densities in Molecules and Crystals, edited by P. BECKER, pp. 791–821. New York: Plenum Press.
GELLER, S. (1958). Acta Cryst. 11, 565–566.
GELLER, S. & WOOD, E. A. (1956). Acta Cryst. 9, 563–568.
GLAZER, A. M. (1972). Acta Cryst. B28, 3384–3392.
GLAZER, A. M. (1975). Acta Cryst. A31, 756–762.
GOODENOUGH, J. B. & LONGO, J. M. (1970). Crystallographic and Magnetic Properties of Perovskite and Perovskite-Related Compounds. Landolt-Börnstein Tabellen, edited by K.-H. HELLWEGE, New Series III/4a, pp. 126–314. Berlin: Springer-Verlag.
HALL, S. R., FLACK, H. D. & STEWART, J. M. (1992). Xtal3.2 Reference Manual. Univs. of Western Australia, Australia, and Maryland, USA.
HESTER, J. R., MASLEN, E. N., SPADACCINI, N., ISHIZAWA, N. & SATOW, Y. (1993). Acta Cryst. B49, 967–973.
HIRSHFELD, F. L. (1977). Isr. J. Chem. 16, 198–201.
KOLB, E. D., WOOD, D. L. & LAUDISE, R. A. (1968). J. Appl. Phys. 39, 1362–1364.
LARSON, A. C. (1970). Crystallographic Computing, edited by F. R. AHMED. Copenhagen: Munksgaard.

MAREZIO, M., REMEIKA, J. P. & DERNIER, P. D. (1970a). Acta Cryst. B26, 300–302.

MAREZIO, M., REMEIKA, J. P. & DERNIER, P. D. (1970b). Acta Cryst. B26, 2008–2022.

MASLEN, E. N. & SPADACCINI, N. (1993). Acta Cryst. A49, 661–667.

MASLEN, E. N., STRELTSOV, V. A., STRELTSOVA, N. R. & ISHIZAWA, N. (1994). Acta Cryst. B50, 435–441.

MASLEN, E. N., STRELTSOV, V. A., STRELTSOVA, N. R. & ISHIZAWA, N. (1995). Acta Cryst. B51, AS682.

MASLEN, E. N., STRELTSOV, V. A., STRELTSOVA, N. R., ISHIZAWA, N. & SATOW, Y. (1993). Acta Cryst. B49, 973–980.

NATHANS, R., PICKART, S. J., ALPERIN, H. A. & BROWN P. J. (1964). Phys. Rev. A, 136, 1641–1647.

O'KEEFFE, M. & HYDE, B. G. (1977). Acta Cryst. B33, 3802–3813.

O'KEEFFE, M. & HYDE, B. G. (1985). An Alternative Approach to Non-Molecular Crystal Structures With Emphasis on the Arrangements of Cations. Structure and Bonding, Vol. 61, pp. 77–144. Berlin: Springer-Verlag.

REES, B. (1977). Isr. J. Chem. 16, 180–186.

REMEIKA, J. P. (1956). J. Am. Chem. Soc. 78, 4259–4260.

REMEIKA, J. P. & KOMETANI, T. Y. (1968). Mat. Res. Bull. 3, 895–900.

SATOW, Y. & IITAKA, Y. (1989). Rev. Sci. Instrum. 60, 2390–2393.

TOFIELD, B. C. & FENDER, B. E. F. (1970). J. Phys. Chem. Solids, 31, 2741–2749.

ZACHARIASEN, W. H. (1967). Acta Cryst. A23, 558–564.

Electron Density and Optical Anisotropy in Rhombohedral Carbonates. III.* Synchrotron X-ray Studies of CaCO3, MgCO3 and MnCO3

BY E. N. MASLEN, V. A. STRELTSOV† AND N. R. STRELTSOVA

Crystallography Centre, University of Western Australia, Nedlands 6907, Australia

AND N. ISHIZAWA

Research Laboratory of Engineering Materials, Tokyo Institute of Technology, 4259 Nagatsuta, Midori-Ku, Yokohama 227, Japan

Abstract

Diffraction-deformation electron-density $(\Delta\rho)$ images for small, naturally faced single crystals of synthetic calcite $(CaCO_3)$, magnesite $(MgCO_3)$ and mineral rhodochrosite $(MnCO_3)$ were measured with focused $\lambda = 0.7$ and 0.9 Å synchrotron (SR) X-radiation. Mo $K\alpha$ $(\lambda = 0.71073$ Å) structure factors were also measured for $MnCO_3$. Lattice mode frequencies predicted from eigenvalues of $\mathbf{T}$ and $\mathbf{L}$ tensors for CO_3 rigid-group motion in these structures are close to spectroscopic values. High approximate $\Delta\rho$ symmetry around the cations increases towards $6/mmm$ in the sequence $CaCO_3$, $MgCO_3$ to $MnCO_3$. The $\Delta\rho$ topography near the CO_3 groups shows the influence of the cations, and correlates strongly with the refractive indices, as required for a cause and effect relationship between electron density and optical anisotropy. Aspherical electron density around the Mn atom can be attributed to the effect of a non-ideal octahedral crystal field on the $3d$ electron distribution. The relationship of the $\Delta\rho$ topography near the Mn atom with that near the CO_3 group in $MnCO_3$ is consistent with magnetic interactions. Space group $R\bar{3}c$, hexagonal, $Z = 6$, $T = 295$ K: $CaCO_3$, $M_r = 100.09$, $a = 4.988(2)$, $c =$

$17.068(2)$ Å, $V = 367.8(3)$ Å^3, $D_x = 2.711$ Mg m^{-3}, $\mu_{0.7} = 1.93$ mm^{-1}, $F(000) = 300$, $R = 0.015$, $wR = 0.012$, $S = 3.0$ for 437 unique reflections; $MgCO_3$, $M_r = 84.31$, $a = 4.632(1)$, $c = 15.007(2)$ Å, $V = 278.8(2)$ Å^3, $D_x = 3.013$ Mg m^{-3}, $\mu_{0.9} = 0.99$ mm^{-1}, $F(000) = 252$, $R = 0.015$, $wR = 0.021$, $S = 4.34$ for 270 unique reflections; $MnCO_3$, $M_r = 114.95$, $a = 4.772(3)$, $c = 15.637(3)$ Å, $V = 308.4(4)$ Å^3, $D_x = 3.713$ Mg m^{-3}, $\mu_{0.7} = 5.62$ mm^{-1}, $F(000) = 330$, $R = 0.015$, $wR = 0.039$, $S = 3.38$ for 386 unique reflections of the SR data set and $a = 4.773(1)$, $c = 15.642(1)$ Å, $V = 308.6(1)$ Å^3, $D_x = 3.711$ Mg m^{-3}, μ(Mo $K\alpha$) $= 5.86$ mm^{-1}, $R = 0.017$, $wR = 0.024$, $S = 2.79$ for 368 unique Mo $K\alpha$ reflections.

Introduction

The birefringence of mineral carbonates, indicating the direction-dependent response of electrons to electric components of light waves, has been modelled repeatedly since the pioneering investigation (Bragg, 1924). We seek an atomic scale explanation for the optical anisotropy $(< n > /n)$ of the rhombohedral carbonates listed in Table 1 that correlates with mean refractive index $(< n >)$, but not with cell volume or a/c ratio. The refractive index n_e* for the electric vector along

---

* Parts I and II: Maslen, Streltsov & Streltsova (1993a,b).

† Author to whom correspondence should be addressed.

---

* The subscripts 'o' and 'e' denote, respectively, the ordinary and extraordinary components of light.